Measurements of the Performance of a Beam Condition Monitor Prototype in a 5 GeV Electron Beam

M. Hempel[h,c,*], K. Afanaciev[d], P. Burtowy[b], A. Dabrowski[b], H. Henschel[c], M. Idzik[a], O. Karacheban[h], W. Lange[c], J. Leonard[c], I. Levy[g], W. Lohmann[h,c], B. Pollak[e], D. Przyborowski[a], V. Ryjov[b], S. Schuwalow[c], D. Stickland[f], R. Walsh[c], A. Zagozdzinska[b]

[a] *AGH University of Science and Technology, Cracow 30-059, Poland*
[b] *CERN, Geneva 1211, Switzerland*
[c] *DESY, Zeuthen 15738, Germany*
[d] *NCPHEP, Minsk 220040, Belarus*
[e] *Northwestern University, Evanston, Illinois 60208, USA*
[f] *Princeton University, Princeton, New Jersey 08544, USA*
[g] *Tel Aviv University, Tel Aviv 6997801, Israel*
[h] *Brandenburg University of Technology Cottbus-Senftenberg, Cottbus 03013, Germany*

Abstract

The Fast Beam Conditions Monitor, BCM1F, in the Compact Muon Solenoid, CMS, experiment was operated since 2008 and delivered invaluable information on the machine induced background in the inner part of the CMS detector supporting a safe operation of the inner tracker and high quality data. Due to the shortening of the time between two bunch crossings from 50 ns to 25 ns and higher expected luminosity at the Large Hadron Collider, LHC, in 2015, BCM1F needed an upgrade to higher bandwidth. In addition, BCM1F is used as an on-line luminometer operated independently of CMS. To match these requirements, the number of single crystal diamond sensors was enhanced from 8 to 24. Each sensor is subdivided into two pads, leading to 48 readout channels. Dedicated fast front-end ASICs were developed in 130 nm technology, and the back-end electronics is completely upgraded. An assembled prototype BCM1F detector comprising sensors, a fast front-end ASIC and optical analog readout was studied in a 5 GeV electron beam at the DESY-II accelerator. Results on the performance are given.

Keywords: CMS, Diamond, Detector, Beam Monitoring, Luminosity

1. Introduction

The fast beam conditions monitor, BCM1F [1], delivers data about the machine induced background to the CMS and LHC control rooms, en-

*Corresponding author at DESY, 15738 Zeuthen, Germany.
Tel.:+49 4089987655
E-mail address: maria.hempel@desy.de

sures a safe operation of the inner tracking detectors, and contributed for high quality data taking. The excellent time resolution of BCM1F of about 1 ns allows to discriminate between machine induced background particles and collision products.

BCM1F was successfully operated during the first running period up to 2012. It was comprised of 8, diamond sensors positioned at a radius of about 4.5 cm around the beam pipe in two planes perpendicular to the beam on both ends of and 1.8 m away from the interaction point. The sensors were equipped with fast and radiation hard front-end, FE-, ASICs with a peaking time of 25 ns and an analog optical readout chain.

At the back-end the signals were split and fed into sampling Analog-to-Digital Converters, ADCs, for the performance monitoring of the device as well as to discriminators. The discriminator output signals were mapped to a time window corresponding to a full turn of relativistic particles around LHC. This allows to assign the counted particles to individual bunches. Gated counting was used to separate machine induced background from collision products. The rate of collision products was used for on-line luminosity measurement, independent from the central CMS data acquisition.

In 2015, the energy of the LHC has be enhanced by a factor of almost 2 and, in addition, the time between two bunch crossings is reduced from 50 ns to 25 ns. Therefore, an upgrade of the beam condition monitors is required [2, 3]. To tackle the higher rates the sensors were subdivided in two pads being read-out individually.

Also a dedicated FE-ASIC with 7 ns peaking time and a signal width of 9 ns at half maximum was developed. The back-end electronics was redesigned and replaced by a dead-timeless histogramming unit with 6.25 ns binning and a 1.25 Gs/s real time digitizer is in development. Again sampling ADCs are used for performance monitoring.

2. Layout of the Upgraded BCM1F

A sketch of a quarter of the BCM1F detector and the Pixel Luminosity Telescope, PLT, is shown in Figure 1.

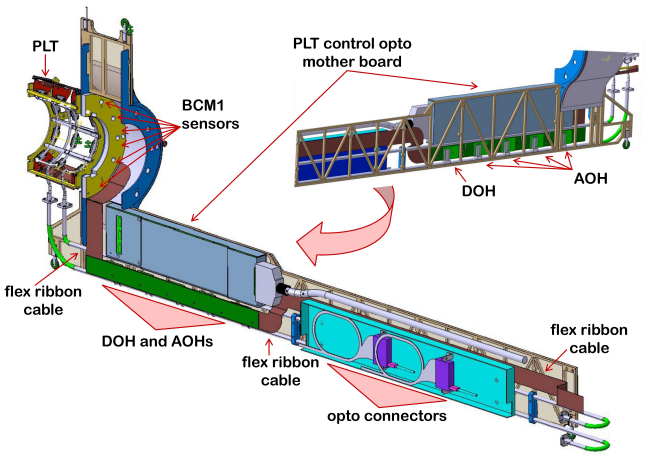

Figure 1: The layout of a quarter of the very forward instrumentation inside CMS. The C-shaped PCB of BCM1F, mounted together with the PLT on a titanium frame, carries diamond sensors and FE-ASICs. The AOH boards transform electrical into optical signals.

Seen from the Interaction Point (IP) the three planes of the PLT are followed by BCM1F. Shown is a half-ring, made of an eight layer rigid C-shaped PCB continued by a flexible part of 1.9 m length. The half-ring carries sensors, FE-ASICs and passive components. The six sensors are positioned in azimuthal angle steps of 30°. Each sensor is metallized with two pads, resulting in 12 readout channels.

The whole BCM1F detector consists of four such half rings, positioned at 1.8 m distance at each end of the IP, with the sensors at a radius of 6.94 cm from the beam axis. The signals are transferred via the flexible PCB to custom-designed laser driver ASICs [4, 5], which modulate the current of the edge-emitting laser diodes. The analog optical signals are transferred to the back-end electronics via single mode fibers.

At the back-end side the signals are converted to electrical signals using an opto-receiver module. They are distributed to discriminators with a double pulse resolution of 7 ns and to two independent digitizer systems in VME and Micro Telecommunications Computing Architecture, μTCA, standard.

The fast digitizer in μTCA standard with 1.25 Gs/s [6] will be used to replace the sampling ADC for performance monitoring, and when fully commissioned, for a more precise sampling of the time.

The discriminator output signals are fed in a look-up table to form coincidence between certain channels. They are also sent to a dead-time free histogramming unit [7] which maps the arrival time of the signals to a time interval of one LHC turn (89 μs). A binning of 6.25 ns is used.

2.1. Diamond Sensors

Single crystal scCVD diamond sensors, produced by chemical vapor deposition by element6 [8] are used. The sensor area is roughly 5x5 mm^2 and the thickness is about 0.5 mm. The sensor surfaces are evened by reactive ion etching and metallized with a tungsten-titanium alloy (90:10 weight ratio) of 100 nm thickness.

Two different sensors were used for the test-beam. One of the sensors is metallized with one pad of 4x4 mm^2 on each side and serves as a reference sensor. The second sensor has a metallization subdivided into two pads of 2x4 mm^2 (CMS design) with a gap of 5 μm in between, as shown in Figure 2.

Figure 2: A photograph of a metallized diamond sensor (left) and a zoom of the gap between the two pads (right).

Prior to the measurements in the test-beam for each sensor the leakage current and the charge collection efficiency, CCE, were measured. The CCE is defined as

$$\mathrm{CCE} = \frac{\mathrm{Q_M}}{\mathrm{Q_G}}, \quad (1)$$

where $\mathrm{Q_M}$ is the charge measured in the sensor and $\mathrm{Q_G}$ the charge expected from the energy deposited by a particle crossing the sensor. $\mathrm{Q_M}$ is obtained from the integral over the signal amplitude as a function of time multiplied by a calibration factor to convert ADC counts into charge. $\mathrm{Q_G}$ is calculated using the energy deposited by an electron from a ^{90}Sr source in the sensor and an energy of 17 eV to create an electron-hole pair in diamond [9]. This value, with a relative uncertainty of 16 %, is slightly larger in comparison to other measurements [10, 11] but consistent with the results presented here.

The thickness of each sensor is measured with a precision of 6 μm using a laser scanning microscope.

The CCE is measured using electrons from a ^{90}Sr source triggered by two consecutive scintillators ensuring that only signals from the high energy tail of the ^{90}Sr spectrum are measured. The CCE measurement setup has a systematic error of 2 %.

The leakage current as a function of the bias voltage for the one-pad sensor is in the order of 10 pA up to 500 V and flat as shown in Figure 3(a). Figure 3(b) displays the CCE as a function of bias voltage that reaches a saturation of 95 % above 160 V.

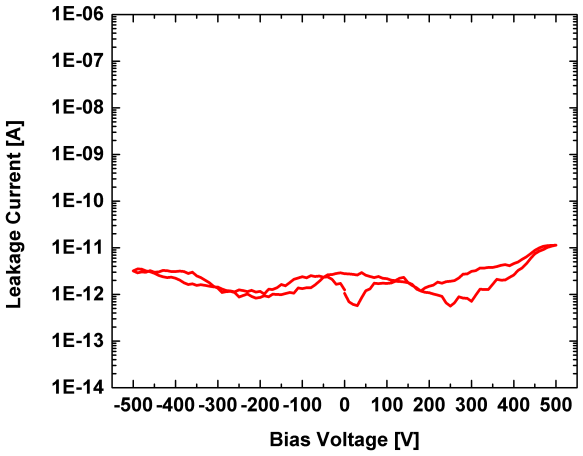

(a) The leakage current of the one-pad sensor as a function of the applied voltage.

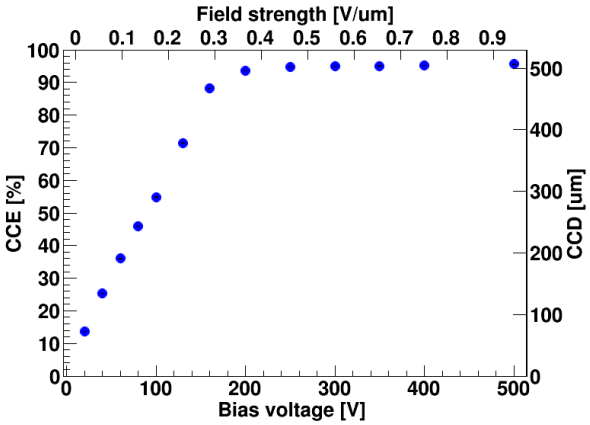

(b) The charge collection efficiency of the one-pad sensor as a function of the applied voltage. The scale on the right side, called charge collection distance (CCD), is the product of the charge collection efficiency and the detector thickness.

Figure 3: Characterization measurements of the one pad diamond done in the laboratory.

A larger leakage current of about 50 pA is observed in the two-pad sensor at 500 V as shown inFigure 4(a).

The CCE as a function of bias voltage is given in

Figure 4(b). It approaches 80 % above 200 V[1].

2.2. FE-ASICS

A dedicated FE-ASIC has been developed in commercial 130 nm CMOS technology [12]. It includes a fast trans-impedance preamplifier with an active feedback, a shaper stage and a fully differential output buffer.

The design goals were linearity up to 10 fC input signal, a gain of 50 mV/fC with an equivalent noise of less than 1000 electrons, a quasi-Gaussian pulse shape with a full-width at half maximum of less than 10 ns and a short recovery time for input signals above the linear range.

These parameters were verified in laboratory measurements. The pulse shape for an injected charge corresponding to the signal of a minimum ionizing particle of about 3 fC is shown in Figure 5(a). A peaking time of 7 ns, a width of 9 ns at Half Maximum, FWHM, and an equivalent noise of less than 400 electrons were measured.

Figure 5(b) illustrates the pulse shape of a 50 times larger charge (150 fC) having a FWHM of less than 10 ns.

The ASIC is provided with an internal calibration circuit. An integrated capacitor of 60 fF feeds a defined input charge to the preamplifier depending on the applied voltage step. A programmable switch defines this pulse height being either 50 mV or 100 mV. An external strobe signal triggers the step.

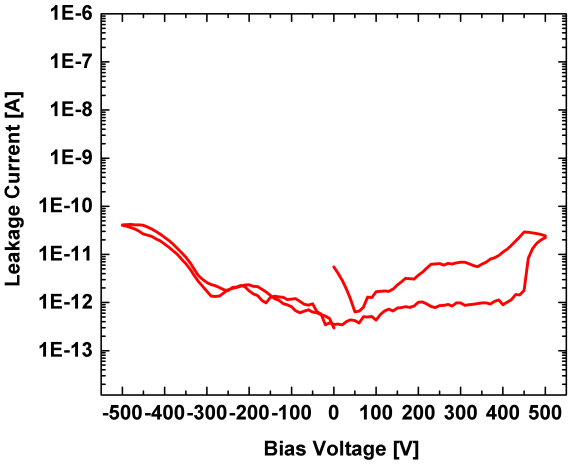

(a) The leakage current of the two-pad sensor as a function of the applied voltage. The two pads were connected to each other resulting in a one pad configuration.

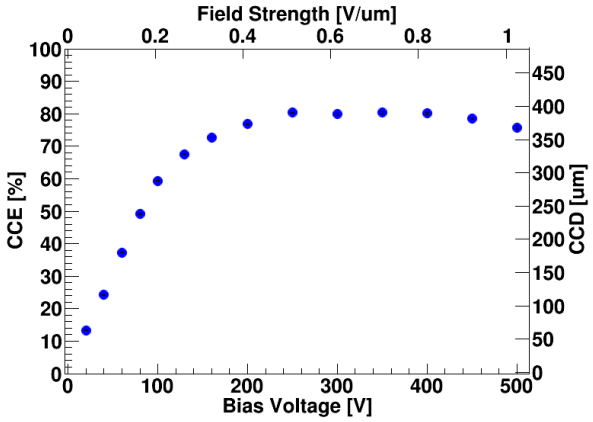

(b) The charge collection efficiency of the two-pad sensor as a function of the applied voltage measured with the two pads connected.

Figure 4: Characterization measurements of the two pad diamond done in the laboratory.

[1]The drop of the CCE value above 400 V is due to a broadening of the pedestal and signal distribution, caused by short baseline fluctuations. This points to erratic currents in the sensor. This behavior was observed already at lower voltages for the opposite polarity in the CCE measurement.

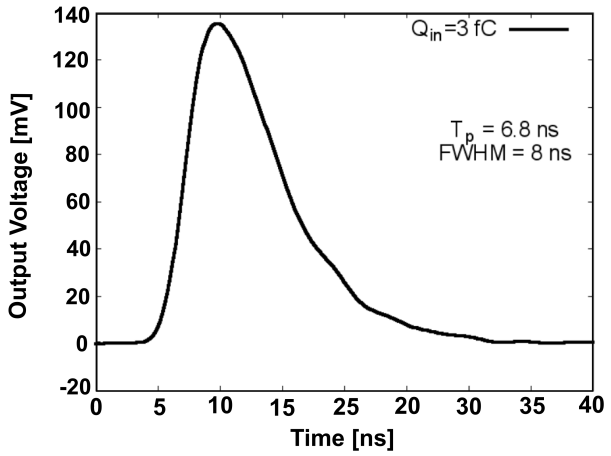

(a) Response of the FE-ASIC to a test charge corresponding to the signal of a minimum-ionizing particle of 3 fC.

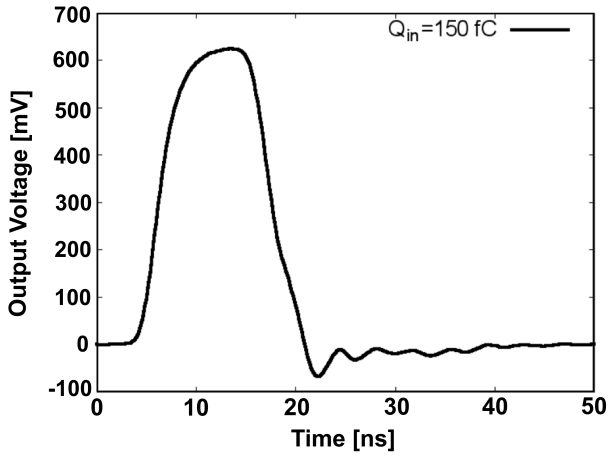

(b) Response of the FE-ASIC to a test charge of 150 fC corresponding to a large signal.

Figure 5: Pulse shapes for different test charges to check the response of the FE-ASIC.

3. Test-Beam Results

3.1. Test-Beam Setup

The test-beam was performed at the DESY-II synchrotron with a secondary electron beam of 5 GeV energy and a rate of about 100 particles per second. The beam size was about 8x8 mm^2. The test-beam facility provides six so called EUDET telescope planes with Minimum Ionizing MOS Active Pixel Sensors, Mimosa-26 [13, 14]. Each telescope plane consists of 576×1152 pixels with a pixel size of 18.4 × 18.4 μm^2.

In the middle of the six telescope planes the Device-Under-Test (DUT) was placed. The DUT consists of a shielding box with a BCM1F prototype comprised of a sensor with one pad and a sensor with two pad metallization, a FE-ASIC and optohybrids. It is mounted on a movable table allowing the positioning of each of the diamond sensors in the center of the beam.

The signal readout from the sensors is triggered by two scintillators located right before the first and two scintillators after the last telescope plane. A schematic of the test-beam setup is shown in Figure 6.

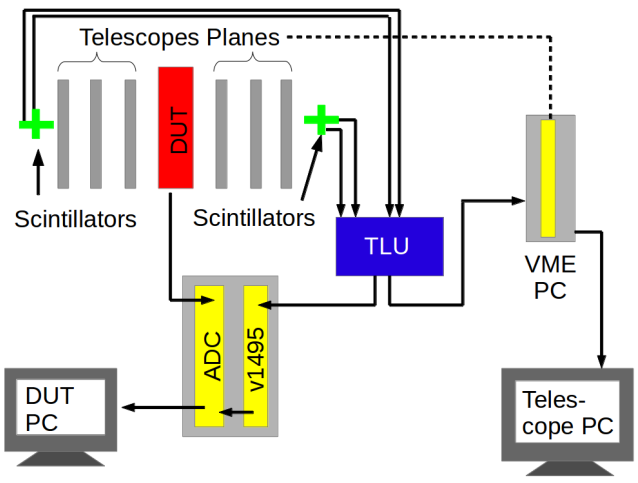

Figure 6: Scheme of the test-beam setup. DUT indicates the position of the detector under test.

The sensor pads are connected with wire bonds to the FE-ASIC input. A picture of prototype PCB in Figure 7 shows the two sensors and the FE-ASICs under a glass cover. The signals of the FE-ASIC are fed into an optohybrid, as used in the final detector which modulates the current of the edge-emitting laser diode. A conversion back to an electrical signal takes place in an analog optical receiver. The reconverted electrical signals are fed into a VME sampling ADC v1721 from CAEN performing 500 MS/s with 8 bit resolution. The ADC data is saved in the DUT computer. A readout trigger for the VME ADC is obtained from a trigger logic unit (TLU) making a coincidence of the scintillator signals. Data coming from all six telescope planes are fed to the VME computer, preprocessed and the files are saved on the telescope computer [15]. To synchronize the readout of the telescope and the VME ADC a CAEN v1495 module [16], sending an unique event number to the telescope and the VME ADC readout, was used. Without the DUT, tracks were reconstructed to align the six telescope planes to each other. Fitting the distribution of the residuals with a Gaussian a value of 2 μm for the standard deviation of the track position was obtained.

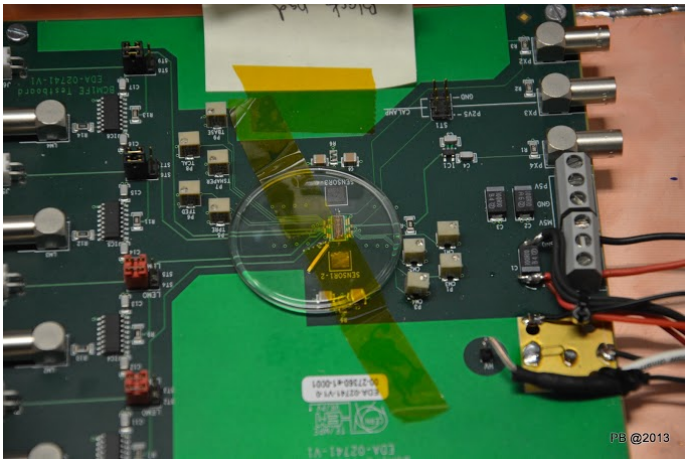

Figure 7: The box containing two diamond sensors and the FE-ASIC protrected under the glass cover.

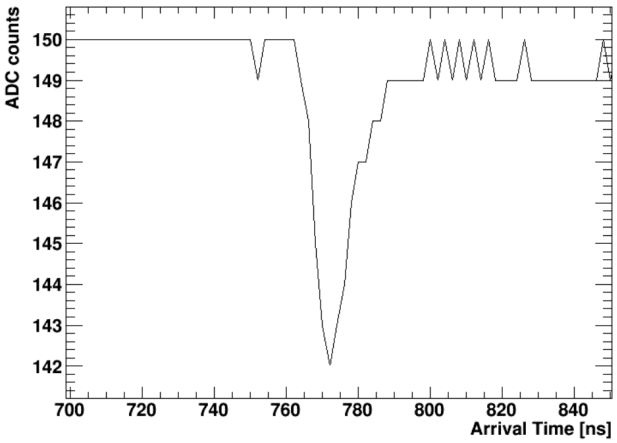

Figure 8: A digitized signal from a pad of the two-pad sensor.

3.2. Signal Shape, Spectra and Signal-to-Noise Ratio

A signal digitized with the VME sampling ADC is shown in Figure 8.

The FWHM of the signal is below 10 ns and the amplitude corresponds to the expectation of a minimum ionizing particle.

Distributing the content of a certain bin outside of the potential signal region for a sample of events measured with the VME ADC, a Gaussian is obtained. Its mean value and the standard deviation are defined as the pedestal and the noise, respectively. The signal amplitude is obtained as the

difference between the maximum of the amplitude of a signal as shown in Figure 8, and the pedestal. A signal amplitude distribution is shown in Figure 9.

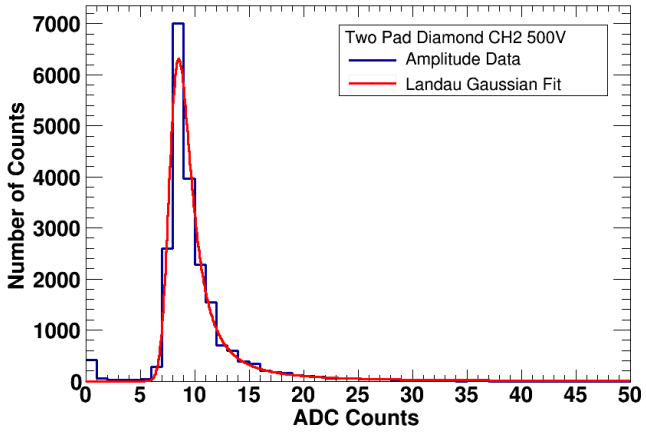

Figure 9: The distribution of the signal amplitudes for one pad of the two-pad sensor.

The shape of the distribution is well described by a convolution of a Landau distribution with a Gaussian with a most probable value as expected from a minimum ionizing particle. These distributions are the same in shape for the one-pad sensor and for each pad of the two-pad sensor.

The ratio of the most probable value of the signal amplitude distribution and the noise, hereafter referred to as signal-to-noise, S/N, ratio, is measured as a function of the sensor voltage and shown in Figure 10 for the one pad sensor and in Figure 11 for the two pad sensor. The one pad sensor reaches a S/N ratio of 40 being almost constant above 250 V. A slightly smaller S/N ratio of 30 is measured for the two pad sensor for both channels being also constant above 250 V. The smaller S/N ratio for the two pad sensor is expected since the charge collection efficiency reaches only 80 %. The difference in channel 1 and channel 2 up to 160 V points to polarization since the CCE values were slightly changing with time and possibly not approaching a constant value in the time of the measurement. This effect is more pronounced at lower bias voltages since then recombination is more likely for a non-perfect sensor.

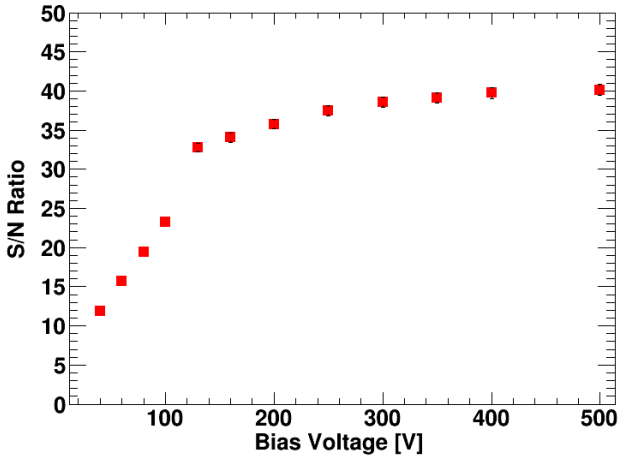

Figure 10: The signal-to-noise ratio as a function of the voltage for the one-pad sensor.

3.3. Homogeneity of the Response and Edge Effects

Using the telescope data the trajectory of each triggered electron is reconstructed and the impact point on the sensor is calculated using the EUTelescope package [17]. The distribution of the impact position on the two-pad sensor is shown, as

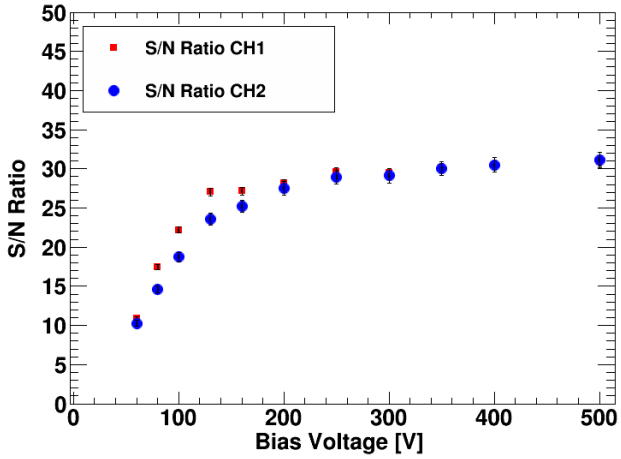

Figure 11: The signal-to-noise ratio as a function of the voltage for the two-pad sensor.

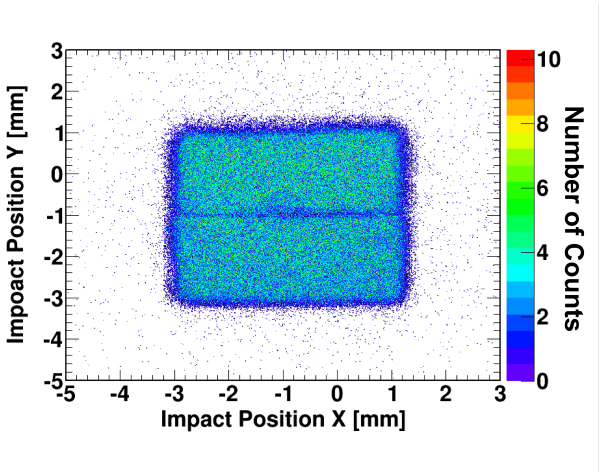

Figure 12: The distribution of the beam-electron impact position on the surface of the two-pad sensor.

an example in Figure 12, for reconstructed tracks to which a signal in the sensor is found in the trigger window larger than the correspondence of 70 % of the CCE. A metallization area of about 4x4 mm^2 is visible in agreement with the expectation from the optical measurements. The density of the impact points is in the central part of the pads almost flat. Near the edges and also near the gap between the pads the density drops.

The CCE as a function of the y-coordinate at a bias voltage of 350 V is shown in Figure 13. It approaches 80 % and is constant over a wide range of the y-position of the beam-electron impact point. The CCE drops at the metallization edge due to a non-homogeneous electrical field at the border leading to distorted signals [10, 18]. A drop of the CCE near the metallization gap over a distance of about 200 μm, much larger than the gap size of 5 μm, is also observed. To understand the relatively wide region of the drop of the CCE near the metallization gap, Ramo's theory [19] was used. A current I_A on a readout electrode A is induced if a charge q moves with a drift velocity $\overrightarrow{v}$ from the starting to the end point by the influence of an electrical field. The corresponding induced charge ΔQ_A is given by the integral of the induced current and is expressed by a so called weighting field $\overrightarrow{E_Q}$ and respectively the weighting potential Φ_A.

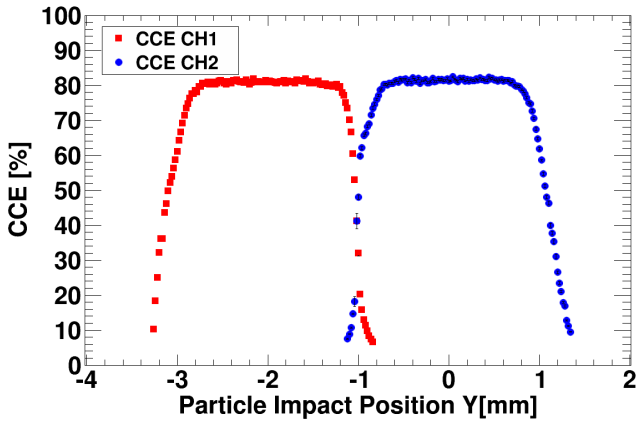

Figure 13: The charge collection efficiency as a function of the y-coordinate along the sensor, operated at 350 V.

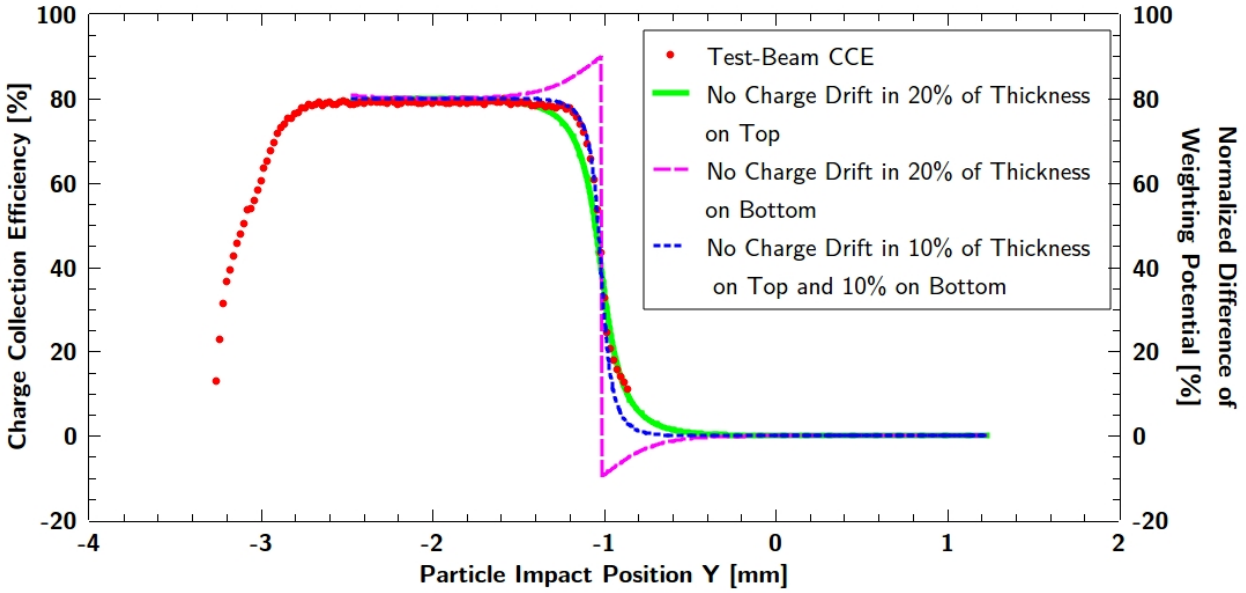

Figure 14: The charge collection efficiency as a function of the y-coordinate measured in one pad of the two-pad sensor and the distribution obtained from the simulation for different drift paths inside the senor.

A weighting potential is obtained if the readout electrode is set to unit potential and all other electrodes to zero potential [20]. The induced current and charge are expressed by:

$$I_A = -q\overrightarrow{v} \cdot \overrightarrow{E_Q} \quad (2)$$

$$\Delta Q_A = q\left(\Phi_A\left(\text{end}\right) - \Phi_A\left(\text{start}\right)\right) \ . \quad (3)$$

Two different cases are considered. First, a charge carrier moves under the readout pad. In this case the weighting field points in the same direction at all positions and the induced current keeps sign at any time. Therefore, the induced charge is a non zero value. In the second case the charge moves under the neighboring pad and the corresponding weighting field changes the sign along the travel path. The induced current changes the sign as a function of time as well and the integral over the time is zero.

However, this is only true for a sensor with 100 % CCE when the charge carrier travels all the way. In the case of a sensor with 80 % CCE the charge carrier does not drift the full path to the electrode, leading to a non-zero integral of the induced current for a charge carrier moving under the neighboring pad.

A simulation was performed using the Poisson Superfish software package [21, 22]. Superfish is a program calculating a static magnetic or electrical field by implementing a sensor geometry. The weighting field and potential is obtained by feeding the simulation with the definition of the weighting field.

For the charge drift in the weighting field three cases are assumed:

- the charge starts drifting at a distance of 20 % of the sensor thickness to the top pad and reaches the lower pad.
- the charge starts drifting at the top pad and disappears at a distance 20 % of the sensor thickness to the bottom pad.
- the charge starts drifting at a distance of 10% of the sensor thickness to the top pad and disappeared at a distance of 10 % of the sensor thickness to the bottom pad.

In all three cases a charge collection efficiency of 80 % is predicted sufficiently far away from the gap. Near the gap, however, the predictions are different, as shown in Figure 14. As can be seen, a moderate description of the measurement can be obtained assuming no charge drift in 20 % of the sensor thickness on the top or in 10 % of the sensor thickness on the top and 10 % on the bottom. Summarizing, the signal size on the two-pad sensor starts to drop at a distance of 200 μm from a 5 μm gap due to 20 % of inefficient material that is at least partially located under the top electrode.

4. Conclusions

A prototype of the upgraded BCM1F detector comprising a scCVD diamond sensor with a two pad metallization, a dedicated fast FE-ASIC in 130 nm technology and an analog optical signal transmission line, has been studied in a 5 GeV electron beam at the DESY-II synchrotron. The output signal of the FE-ASIC, characterized by a peaking time and pulse width of about 7 ns and 9 ns, respectively, is maintained after the full readout chain. The signal-to-noise ratio is measured as a function of the sensor bias voltage. It reaches 30 for a bias voltages larger than 250 V. The response over the sensor area is flat. The CCE for the two-pad sensor used is 80 %. A drop of the CCE is observed near the edges of the pads and near the gap between the two pads, being qualitatively described by a simulation using the Superfish software package.

Acknowledgements

The test-beam was performed within the FCAL collaboration, co funded by the European Commission under the FP7 Research Infrastructures project AIDA, grant agreement no. 262025. Support was also given for some authors by the German-Israeli foundation, GIF. We are grateful to B. G. Harrop from Princeton University and the target laboratory at GSI for performing the metallization of the sensors.

References

[1] A. Bell, et al., Fast Beam Conditions Monitor BCM1F for the CMS Experiment, Nucl. Inst. and Meth. A, 2010 614 (2010) 433–438.

[2] J. L. Leonard et al., Upgraded Fast Beam Condition Monitor for CMS Online Luminosity Measurements, Proceedings of Science (TIPP2014) 346, 2014.

[3] K. K. Gan, Diamond Particle Detectors Systems in High Energy Physics, Proceedings of Science (TIPP2014) 103, 2014.

[4] J. Troska, et al., Optical Readout and Control Systems for the CMS Tracker, IEEE Trans. Nucl. Sci., 2003 50 (2003) 1067–1072.

[5] G. Cervelli, et al., A Radiation Tolerant Laser Driver Array for Optical Transmission in the LHC Experiments, 7th Workshop on electronics for LHC experiments, Stockholm, Sweden, 2001 (2001) 155–159. .

[6] A. Zagozdzinska, Architecure of the Upgraded BCM1F Backend Electronics for Beam Conditions and Luminosity Measurement, TWEPP 2014 - Topical Workshop on Electronics for Particle PhysicsProceedings, to be published in JINST, 2014.

[7] M. Penno, A Real-Time Histogramming Unit for Luminosity and Beam Background Measurements for each Bunch Crossing at the CMS Experiment, TWEPP 2013 - Topical Workshop on Electronics for Particle Physics, Perugia, Italy, 2013.

[8] Element Six Ltd, Kings Ride Park, Ascot, Berkshire, SL5 8BP, UK.

[9] H. Pernegger et al., Measurements of Charge Carrier Properties in Single-Crystal CVD Diamond using the Transient-Current Technique, Journal of Applied Physics, 97, 073704, 2005.

[10] M. Pomorski, Electronic Properties of Single Crystal CVD Diamond and its Suitability for Particle Detection in Hadron Physics Experiments, PhD Thesis, Johann Wolfgang Goethe University, Frankfurt am Main, 2008.

[11] M. Gabrysch et al., Formation of Secondary Electron Cascade in Single-Crystalline Plasma-Deposited Diamond upon Exposure to Femtosecond X-Ray Pulses, Journal of Applied Physics, 103, 064909, 2008.

[12] D. Przyborowski, et al., Development of Front-End Electronics for the BCM1F Diamond Detector Beam Condition Monitor at CMS, ACES 2014 - Fourth Common ATLAS CMS Electronics Workshop for LHC upgrades, CERN, March 18-20, 2014.

[13] J. Baehr, Test Beam Measurements with the EUDET Pixel Telescope, EUDET-Report-2010-01, 2010.

[14] I. Gregor, Summary of One Year Operation of the EUDET CMOS Pixel Telescope, Proceedings, International Linear Collider Workshop, LCWS08, Chicago, USA, November 16-20, 2008.

[15] E. Corrin, The EUDET High Resolution Beam Telescope - The Final Digital Readout, EUDET-Report-2009-06, 2009.

[16] D. G. Cussans, Description of the JRA1 Trigger Logic Unit (TLU), v0.2c, EUDETMemo-2009-04 , 2009.

[17] A. Bulgheroni, et al., EUTelescope: Tracking Software, EUDET-Memo-2007-20, 2007.

[18] E. Berdermann et al., Performance of Diamond Detectors in a Fragmentation Experiment, Proc. XLV Intern. Winter Meeting on Nuclear Physics Conference, Bormio, Italy, 2007.

[19] S. Ramo, Currents Induced by Electron Motion, Proceedings of the IRE 27 p. 584–585. .

[20] H. Spieler, Semiconductor Detector Systems, Oxford Univeristy Press, 2005.

[21] K. Halbach, R. Holsinger, Superfish- A Computer Program for Evalution of RF Cavities with Cylindrical Symmetry, Particle Accelerators Vol. 7, p. 213-222, Gordon and Breach, Science Publisher Ltd. 1976.

[22] J. Billen, L. Young, User‘s Guide for the POISSON/SUPERFISH Group of Codes, LA-UR-96-1834, 2006.